

The effect of spacing on the flow around a pair of roughness cubes resolved by microscopic dual-view tomographic holography

Jian Gao¹, Karuna Agarwal¹, Joseph Katz^{1*}

¹Johns Hopkins University, Department of Mechanical Engineering, Baltimore, USA

*katz@jhu.edu

Abstract

In this study, a recently developed technique, namely microscopic dual-view tomographic holography (M-DTH) is used for high-resolution, three-dimensional (3D) measurement of the flow around a pair of cubic roughness elements in a fully developed turbulent channel flow. The friction Reynolds number is $Re_\tau=2500$, and the cube height, a , is 1 mm, corresponding to 90 wall units ($\delta_v=11 \mu\text{m}$) and 4% of the half channel height 25 mm, h (δ). To investigate the effect of cube spacing, the pair of cubes are aligned in the spanwise direction, and separated by a , $1.6a$, and $2.5a$. M-DTH circumvents the depth-of-focus problem of single-view holography by truncating the elongated particle traces via multiplication of intensity fields reconstructed from the two views. A self-calibration procedure that determines the 3D distortion field is developed for precise matching of the coordinate systems associated with each view. The subsequent 3D particle tracking is based on the guidance velocity field and the truncated particle traces which both are determined from the multiplied intensity fields. Compared to single-view holography, significant improvement in measurement accuracy has been achieved by M-DTH. In addition, the current version of the technique is fully equipped with in-house accelerated data processing using graphics processing units (GPUs), which has achieved significantly speed-up in data processing and hence greatly reduces the processing time of M-DTH for determining turbulence statistics. The flow around individual cubes exhibits similar features for the three cube spacings. The boundary layer separates upstream of the cubes with the formation of horseshoe vortex that rolls up in front of the cube, and then wraps around it, forming a pair of counter-rotating “legs”. A vortical “canopy”, dominated by wall-normal vorticity that forms along the sides of each cube and spanwise vorticity above it, covers the entire roughness element and part of the near wake behind it. Additionally, the flow is asymmetric with respect to the cube center plane for all spacings. On the other hand, the flow structure interaction at regions between the cubes and in the near wake exhibits distinct features at different cube spacings. Stronger horseshoe legs develop between the cubes for narrower spacing. A broad pair of counter-rotating streamwise vortices develop behind each cube, engulfing the adjacent legs of the horse vortex and the secondary streamwise vortex at the outer side. This process occurs in the nearer wake region with decreasing cube spacing. The narrower spacing also results in faster channeling flow between the cubes but faster flow deceleration in the near wake.

Introduction

Considerable efforts have been made to characterize the effects of roughness scales and geometries on the mean flow profile and turbulence statistics (Jimenez 2004, Raupach et al. 1991) as well as the drag and noise generated by the rough surfaces (Yang and Wang 2009, Yang and Wang 2013). In spite of numerous studies, too many to summarize in this paper (Devenport et al. 2018, Flack and Schultz 2014, Yang and Wang 2013), there are no accepted universal relations between the roughness characteristics, including geometry, spacing, and scales, and the wall friction as well as noise generated by the roughness. Limited direct knowledge demonstrating the complex interaction of the boundary layer turbulence with the roughness is available from computational studies, e.g., (Ismail et al. 2018, Yang and Wang 2013), and very few experiments (Hong et al. 2011, Talapatra and Katz 2012). The latter still miss many of the details, especially for the flow between elements.

The flow around cubic roughness elements serves as a convenient model for a study fully resolving the flow-roughness interactions. The flow around “large” ($\delta/a < 5$) surface mounted cube immersed in a turbulent boundary layer has been a popular model for characterizing bluff-body flows (Castro 1977, Martinuzzi and Tropea 1993, Yakhot et al. 2006). For $\delta/a \sim 1$ the cube acts more as an obstacle than a roughness element. Yet, they elucidate some of the main flow features. For example, the flow structures in the vicinity of the cube include a horse-shoe vortex, separation bubbles along the side and top surfaces, and an arch-type vortex in the recirculation region behind the cube (Martinuzzi and Tropea 1993). To the best of our knowledge, there is no experimental data for the flow around cubes embedded in the inner part of the boundary layer, e.g. $\delta/a = 25$, where they mostly represent roughness.

High spatial-resolution is required for measuring the flow field around individual roughness elements at high Reynolds numbers, explaining the scarcity of available data. For example, Hong et al. (2011) use high-magnification particle image velocimetry (PIV) to characterize the roughness sublayer ($\sim y/a < 5$) over an arrays of pyramidal elements with $\delta/a = 50$. In a continuation study, Talapatra and Katz (2012) use digital holographic microscopy (DHM) to resolve the prevalent “U-shaped” vortical structures postulated in (Hong et al. 2011). They conclude that the U-shaped vortices play a significant role in the turbulent wall-normal momentum transport above the pyramidal roughness. Hong et al. (2012) also show that coherent turbulent structures with scales comparable to the roughness height, which are generated as the boundary layer turbulence interacts with the pyramidal elements, play a primary role in the sub-grid energy flux (>50%) in and above the roughness sublayer. These studies demonstrate the significance of understanding the processes involved.

In the present study, we aim at resolving the flow around a pair of roughness cubes embedded in a high Reynolds number channel flow. The roughness and viscous length scale are well separated ($a/\delta_v = 90$), and the cube height is significantly smaller than the half channel height ($\delta/a = 25$). The spacing between cubes, λ , varies between $1-2.5a$. To gain unobstructed access to the flow domain, the measurements are performed in the JHU refractive index matched facility. To achieve high accuracy in 3D velocity measurements, we utilize the recently-developed microscopic dual-view tomographic holography (M-DTH) (Gao and Katz 2018) briefly described in the following sections. Our recent efforts of developing GPU-based code for faster data processing is also described, which

enables M-DTH to be used as a viable tool to determine turbulence statistics from large amount of data. Current flow measurement results provide a detailed picture of the dominant flow mechanisms involved, including the vortical canopy engulfing each cube, deformation of this canopy due to the neighboring cube, and the evolution of horseshoe vortices developing around each element.

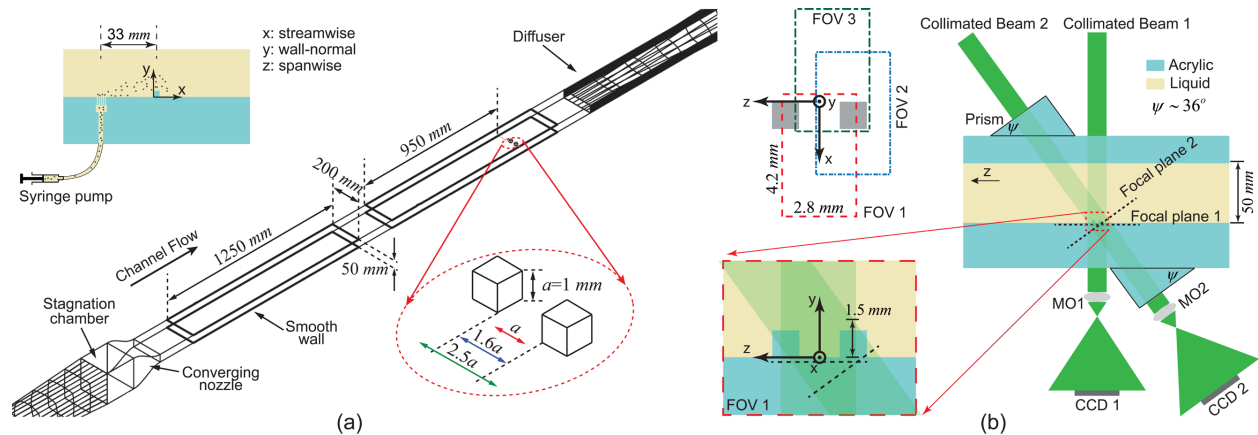


Figure 1: Schematic of experimental facility (a) and M-DTH setup (b). Inset in (a): local particle injection upstream of the cubes. Inset in (b): three field of views (FOV).

2 Methodology

The flow facility and the local tracer particle injection system for flow visualization are shown in Fig. 1(a). The incoming flow is fully developed turbulent channel flow at $Re_\tau = u_\tau h / \nu = 2500$, where $h = 25 \text{ mm}$, is half channel height, u_τ the friction velocity, and ν the kinematic viscosity, respectively (Zhang et al. 2017). The pair of cubes are aligned in the spanwise direction, and have a nominal height of 1 mm , corresponding to 90 wall units ($\delta_\nu = 11 \mu\text{m}$) and $h/a = 25$. Experiments have been performed for cubes separated by $1.0a$, $1.6a$, and $2.5a$. Precision measurements of the cube shape show that because of machining errors, the actual dimensions of the cube and the spacing differ slightly from the nominal values. For the nominal cube spacing of $1.6a$, the actual dimension of the cube is indeed $1.0 \times 1.0 \times 1.0 \text{ mm}^3$ in the streamwise (x), wall-normal (y), and spanwise (z) directions, respectively, but the spacing is 1.55 mm . For the nominal cube spacing of $1.0a$, the actual dimension are $1.04 \times 0.95 \times 1.03 \text{ mm}^3$, i.e. it is slightly shorter in the wall-normal direction, and the spacing is 0.95 mm . For the nominal cube spacing of $2.5a$, the actual dimension are $1.04 \times 0.94 \times 0.96 \text{ mm}^3$, and the spacing is 2.45 mm . To gain unobstructed optical access, the walls of the channel as well as the cubes are made of acrylic whose refractive index is matched with that of the working fluid, a concentrated aqueous solution of sodium iodide (Bai and Katz 2014, Hong et al. 2011). The cube is machined as part of a 110 mm diameter disk that is flush mounted in the channel window. A dense particle suspension is required to resolve the flow structure at scales that are much smaller than the cube. Hence, the $2\text{-}\mu\text{m}$ tracer particles are injected locally upstream of the cubes (Sheng et al. 2008, Talapatra and Katz 2013), as shown in the upper-left inset of Fig. 1(a).

The M-DTH setup is illustrated in Fig. 1(b). The beam of a double-pulse Nd:YAG laser (New Wave Solo PIV) is spatially filtered, collimated, and split to illuminate the sample volume from two angles.

One beam is perpendicular to the channel wall, and the other is nominally inclined at 36° to the perpendicular direction. The region where the two beams overlap is the sample volume, as highlighted in the bottom-left corner of Fig. 1(b). The top-left corner of this Figure indicates that the sample volume is adjusted to concentrate on the flow: (i) between and behind the cubes, corresponding to field-of-view 1 (FOV 1); (ii) upstream of the cubes (FOV 3); and around one of the cubes (FOV 2). The in-line holograms are magnified by two identical 8X microscope objectives (MO1 and MO2), and then recorded by two identical interline-transfer, CCD cameras (Imperx B6640). Each camera has a 6600×4400 -pixel array, with an effective pixel size of $0.68 \mu\text{m}$. The resulting sample volume size, where the analysis is performed, is $4.2 \times 2.8 \times 1.5 \text{ mm}^3$ ($382\delta_v \times 255\delta_v \times 136\delta_v$) in the streamwise, spanwise, and wall-normal directions, respectively. The origin of the experimental coordinate system is located on the wall, between front surfaces of the cubes (see Fig. 1(b)). Instantaneous hologram pairs are acquired by both cameras at a rate of 1.5 Hz with $25 \mu\text{s}$ delay between exposures. Thousands of hologram pairs are recorded to obtain converged statistics of the mean flow fields for each cube spacing and each FOV.

“Conventional” microscopic single-view holographic tracking (Sheng et al. 2008, Talapatra and Katz 2013) has a lower accuracy for velocity measurements in the axial direction of the illuminating beam (depth, wall-normal direction) due to the so-called depth-of-focus (DOF) problem (Katz and Sheng 2010). Hence, it does not have sufficient accuracy to resolve the complex, 3D flows around the cubes, where the wall-normal velocity component varies substantially. This problem has been resolved by developing and implementing the M-DTH system to perform tomographic particle tracking. A detailed description of the M-DTH technique is provided in a recently published paper (Gao and Katz 2018). Briefly, the M-DTH consists of the following steps. (i) Precision mapping of the two sample volumes using a new 3D self-calibration procedure, which accounts for geometric differences and corrects the image distortions. (ii) Reconstructing the two instantaneous 3D intensity fields which contain the elongated traces. (iii) Mapping of the intensity field of one view into the next. (iv) Truncating the elongated particle traces by multiplying the two fields, which reduces the length of the elongated traces to about twice the particle diameter as opposed to 5-20 times without truncation. The precise mapping ensures most of the elongated particle traces overlap near their centers. (v) Particle detection and matching of truncated traces in the two exposures following procedures described in (Sheng et al. 2008, Talapatra and Katz 2013). Unlike before, the matching is based on 3D cross-correlations made possible by the truncated traces. (vi) Measuring the particle displacement and using 1st order singular value decomposition (SVD) (Sheng et al. 2008) for mapping the unstructured velocities onto a regular grid, which also provides the velocity gradient tensor field. By calculating the divergence of the velocity distribution, Gao and Katz (2018) show that the new dual-view tomographic procedures improve the measurement accuracy significantly compared to single-view results.

Previous processing of data using codes written in MATLAB© has been cumbersome and slow. Considering the large image size (6600×4400) as well as various procedures in a series of processing steps, enormous amount of computation is needed to calculate the 3D velocity field from one realization. In addition, considerable data storage is required. For each view and each frame, the hologram is reconstructed at hundreds of planes (with an interval of $4 \mu\text{m}$) to retrieve the whole volume. These reconstructed images are needed in the following processing steps and therefore are saved to hard drives for future use. 50 GB is needed for each realization. To perform self-calibration

using a group of realizations (e.g., 250 realizations), 12 TB is needed. Frequent accessing to hard drives also adds to the total processing time. Also, to perform the sum-of-cross-correlation calculation in the self-calibration step and the 3D cross-correlation calculation in the particle tracking step, the corresponding images are computed by the MATLAB© code then imported to the DaVis© software for displacement calculation, which is cumbersome. The C++ GPU-based code is developed to overcome the disadvantages of previous processing. An important feature of the GPU-based code is that it takes much less time to reconstruct a hologram by GPU than reading the already reconstructed image from a hard drive. Therefore, in the GPU code the hologram is reconstructed whenever needed in different steps and thus no extra storage is required to keep the intermediate files. The GPU-based code takes full advantage of the massive parallel computing capabilities of GPUs and all major processing components in the algorithm are realized in parallel, including but not limited to hologram reconstruction, particle detection, self-calibration, 2D sum-of-cross-correlation, and 3D cross-correlation. The GPU-based cross-correlation codes are able to perform 2D and 3D multi-grid, multi-pass correlation calculations and hence can be used as standalone tools for processing planar and tomographic PIV images and retrieving vector fields. Benchmark tests on the performance of the developed GPU-based code are performed and results of three processing steps for one realization are listed in Table 1 as examples. Note, the MATLAB© code is running on a machine with Intel© i9-7920X CPU (4.3 GHz, 24 threads) and is comparing with the C++ GPU-based code running on NVIDIA© RTX 2080 Ti (1.5GHz, 4352 CUDA cores). With all processing steps combined, it takes the CPU-based code 310 minutes to process one realization, while for the GPU-based code, 22 minutes. Therefore, an overall speed-up of 14X has been achieved. Further speed-up is available as we gain more experience in optimizing the code. In particular, more advanced GPUs with larger global memories are beneficial to further speed-up because the sample volume can be divided into bigger but fewer sections for the calculation.

Table 1: Benchmark results of three example processing steps showing the processing times used by the CPU-based and GPU-base codes

	Hologram reconstruction and particle detection	Self-calibration: Mapping from view2 to view1 and sum-of-cross-correlation	Intensity field mapping and multiplication, 3D cross-correlation
CPU-based code	4393 seconds	598 seconds	120 minutes
GPU-based code	51 seconds	17 seconds	10.7 minutes
Speed-up	86X	35X	11X

Processing of the vast amount of data collected is still in progress. For λ of $1.0a$, the present discussion is based on 844 and 886 instantaneous realizations of FOV 1 and 2, respectively. For λ of $1.6a$, we use 1442 and 152 realizations obtained for FOV 1 and 2. For λ of $2.5a$, we use 89 realizations obtained for FOV 2. For each case, the mean velocity field is calculated by combining all the unstructured vectors, and then projecting them on a regular grid using SVD. For each grid point, the velocity and its gradients are calculated based on the unstructured values located with a sphere centered on this point. The radius is chosen to ensure that at least 15 unstructured vectors can be found within the sphere for each grid point. The current sphere diameter is 100 μm , but is larger for fewer realizations, e.g., for λ of $2.5a$, the diameter of the sphere is 180 μm . The distance between neighboring grid points is 60 μm in all directions. The calculated velocity field is further smoothed to reduce the outliers due to insufficient unstructured vectors. As our database increases by

processing additional realizations (in progress), the sphere size as well as the vector spacing will be further reduced.

3 Results and Discussion

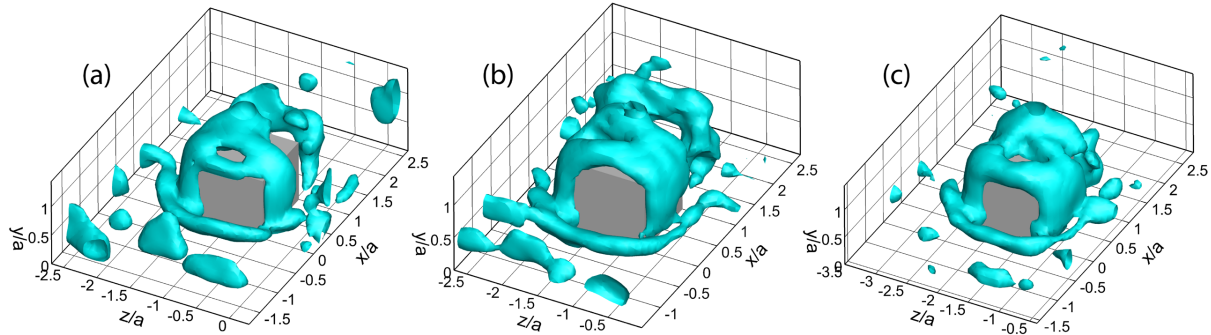


Figure 2: Iso-surface of $\lambda_2 = -8.0 \times 10^5 \text{ s}^{-2}$ for λ of $1.0a$ (a), $1.6a$ (b), and $2.5a$ (c).

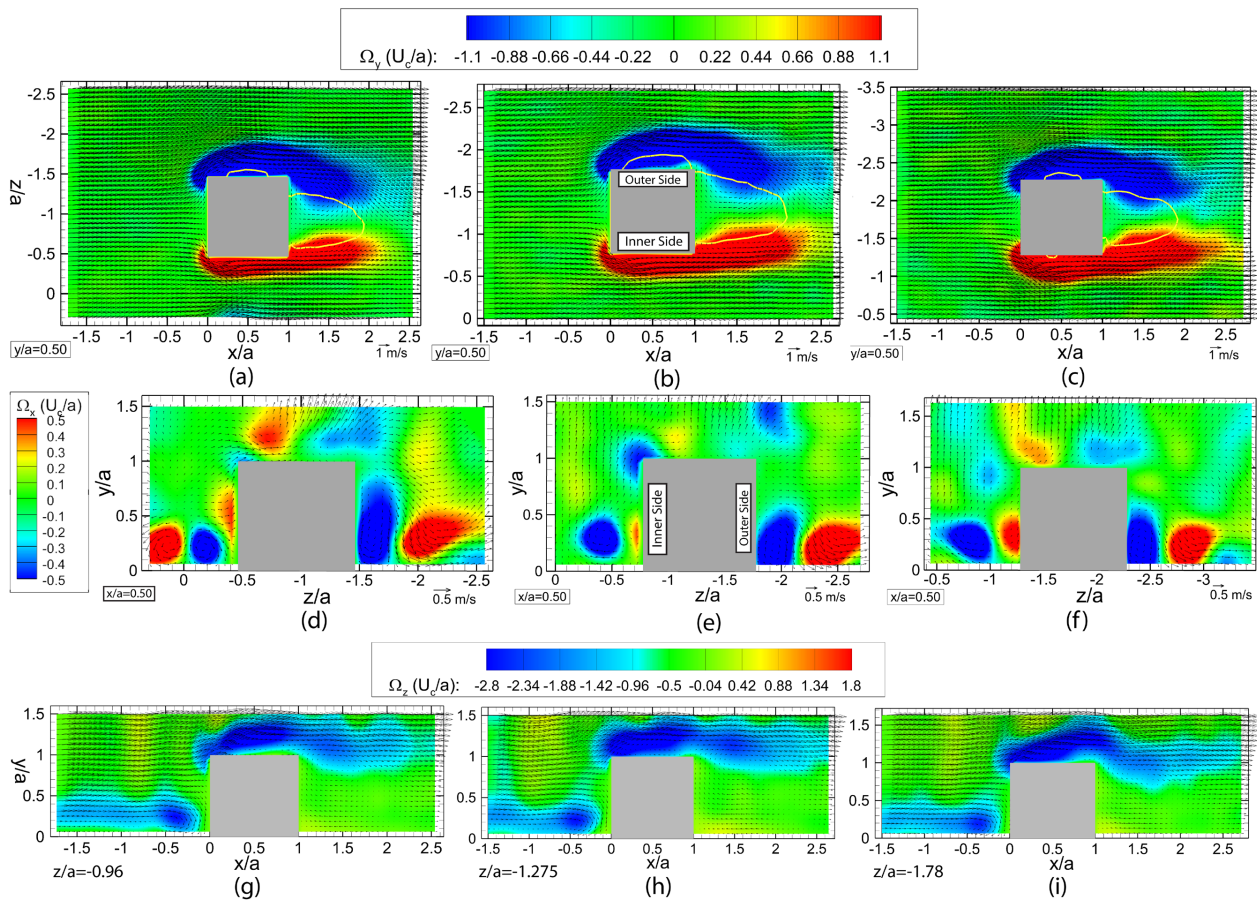


Figure 3: Vorticity (color) and velocity (vectors) distribution on cube-center planes. (a)-(c) wall-normal vorticity (Ω_y) and x-z velocity on plane $y/a=0.5$. (d)-(f) streamwise vorticity (Ω_x) and y-z velocity on plane $x/a=0.5$. (g)-(i) spanwise vorticity (Ω_z) and x-y velocity on plane $z/a=-0.96$ (g), -1.275 (h), and -1.78 (i). U_c : channel center-line velocity. The yellow lines in (a)-(c) are contour lines where the streamwise velocity is zero. Inner side: the side of the cube nearer to the neighboring cube; Outer side: the further side from the neighboring cube.

The vortical structures around one cube are visualized by iso-surface of λ_2 (Jeong and Hussain 1995), as shown in Fig. 2, where the flow around individual cubes exhibits similar features for the three spacings. The vorticity and velocity distributions on planes that cut through the cube center are shown in Fig. 3. The boundary layer separates upstream of each cube (Figs. 3g-i), causing formation of a horseshoe vortex that rolls up in front of the cube, and then wraps around it, forming a pair of counter-rotating “legs” (Figs. 3d-f). A vortical “canopy”, dominated by wall-normal vorticity along the sides of each cube (Figs. 3a-c) and spanwise vorticity above it (Figs. 3g-i), covers the entire cube and part of the near wake behind it, appearing as an arch surrounding the recirculation region. The canopy is asymmetric with respect to the cube center due to influence of the neighboring canopy, as evidenced by asymmetric velocity and vorticity distribution (Figs. 3a-f). As the cube spacing decreases, the flow is increasingly asymmetric. In particular, for the $1.0a$ spacing (Fig. 3d), the horseshoe legs at the inner side as well as the secondary streamwise vortex between the cube side wall and the horseshoe leg are significantly different from those at the outer side. Flow separates and reattaches at the cube outer side, as shown in Figs. 3(a)-(c). By reducing the interpolation volume using more data, the separation region at the inner side is also resolved (data not shown here), whose size in the spanwise direction is less than $30 \mu\text{m}$. Flow separation and reattachment also occurs on the cube top surface.

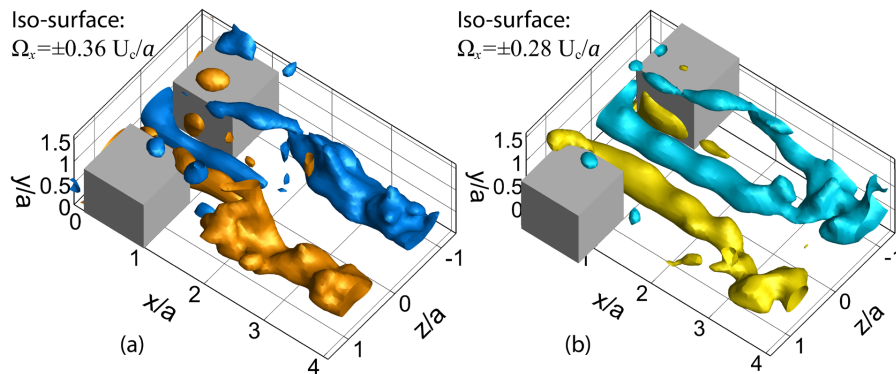


Figure 4: Iso-surface of Ω_x for λ of $1.0a$ (a) and $1.6a$ (b).

The flow interaction at regions between the cubes and in the near wake exhibits distinct features at different cube spacings, as shown in Figure 4. The streamwise vortices at narrower spacing are significantly stronger than the wider spacing case. To investigate the evolution of the streamwise vorticity downstream, different cross-section of the streamwise structures are shown in Figure 5. In addition to the counter-rotating horseshoe legs between the cubes, a pair of counter-rotating vortices develop at the cube top edge at the inner side, which are much stronger for the narrower spacing, as shown in Figs. 5(a) and 5(b). At $x/a \sim 1.80$, for the narrower spacing (Fig. 5c), the horseshoe legs between the cubes are attenuated significantly. A broad pair of counter-rotating structures, which originate from the vortex developed at the cube top edge (Fig. 5a) and the secondary streamwise vortex at the outer side (not shown here), appears behind the cube and starts to entrain the horseshoe leg. The merged streamwise vortical structures further intensifies downstream, as shown in Fig. 5e. In contrast, for λ of $1.6a$, the vortex developed at the cube top edge is much weaker (Fig. 5b) and the horseshoe legs between the cubes maintain (Fig. 5d) until $x/a \sim 2.50$. As shown in Fig. 5f, a broad pair of counter-rotating vortices entrain the horseshoe legs.

This process is similar to that in the narrower spacing case but occurs further downstream at wider spacing.

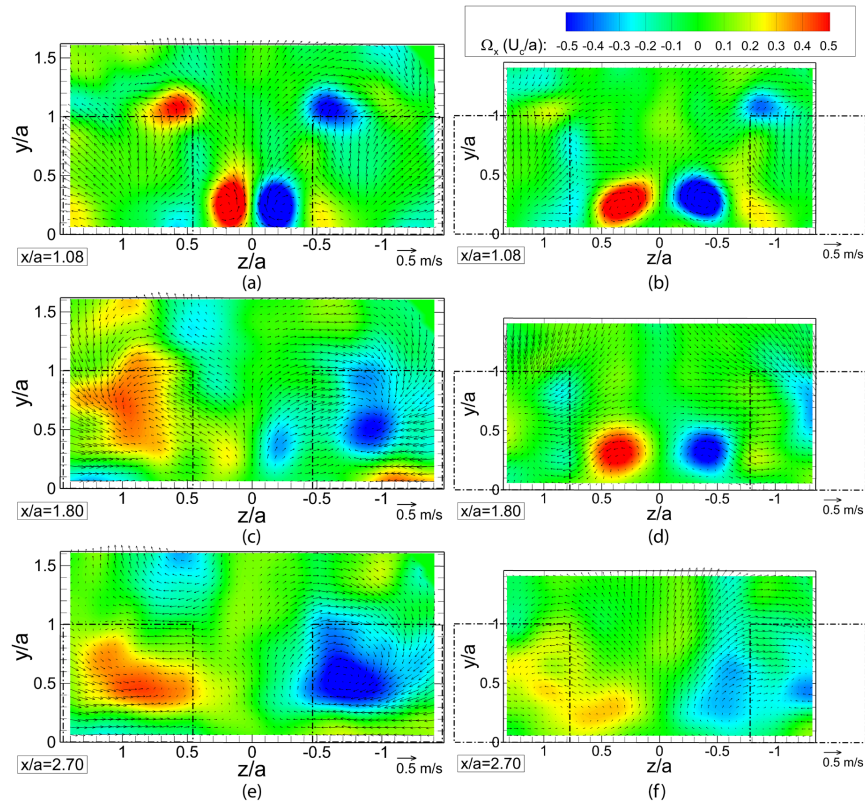


Figure 5: The y - z velocity distributions superimposed on streamwise vorticity in planes $x/a=1.08$ (a and b), 1.80 (c and d), and 2.70 (e and f) for λ of $1.0a$ (left column) and $1.6a$ (right column).

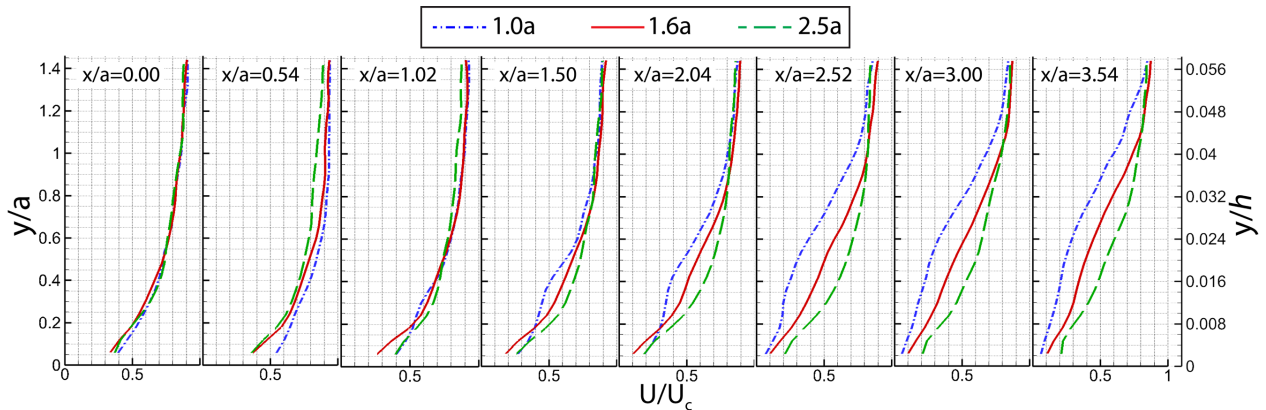


Figure 6: Streamwise evolution of streamwise velocity on the center plane ($z=0$) between the two cube. U_c is the center line velocity at half the channel height.

The difference in velocity gradient also contributes to the difference in the interaction of flow structures. The effect of cube spacing on flow channeling is characterized in Fig. 6 by comparing the evolution of streamwise velocity profile on the middle plane ($z=0$). Between the cubes ($0 < x/a < 1$) the velocity near the channel wall is higher than that occurring further downstream. With

decreasing spacing, the channeling increases, i.e. the streamwise velocity becomes significantly larger. This trend is reversed at $x/a > 1$, where the streamwise velocity corresponding to the wider gap decreases at a slower pace. The latter trend might be attributed to the flow induced by the previously-discussed large counter-rotating streamwise vortices, which deplete the high-streamwise momentum from the center near-wall region at a faster pace for the narrower gap. The significant deceleration that occurs for the narrower gap contracts the vortex line in the streamwise direction and hence contributes to the attenuation of the horseshoe legs.

4 Conclusion

The microscopic dual-view tomographic holography (M-DTH) is applied to measure the flow around a pair of roughness cubes immersed in the inner part of a turbulent channel flow. Recent upgrade of the technique involves acceleration in data processing achieved by the newly developed GPU-based code, such improvement enables the technique to be used as a viable tool for determining turbulence statistics via processing of large amount of data. In order to study the effects of spacing on the flow, data has been taken, processed, and analyzed for three cube spacings. The boundary layer separates upstream of the cube and rolls into a horseshoe vortex that wraps around the sides of the cube. A vortical canopy, dominated by the wall-normal vorticity along the side walls and spanwise vorticities above the cube, engulfs almost the entire cube. It connects with an arch-type vortex that develops behind the cube. Flow separation regions with reverse streamwise velocity form on all the surfaces, but the width of these regions is significantly smaller between the cubes. The presence of a neighboring cube introduces asymmetry in the flow surrounding the cube. The horseshoe vortices persist only a short distance behind the cubes, which decreases with decreasing spacing, and are entrained by much larger streamwise structures. These structures develop earlier, and appear to increase in strength with decreasing cube spacing. The ongoing analysis will not only provide higher-resolution data, it will also be used for characterizing the effects of the phenomena described in this paper on the structure of turbulence around the cubes.

Acknowledgements

This work has been supported by the Office of Naval Research.

References

- Bai KL, and Katz J (2014) On the refractive index of sodium iodide solutions for index matching in PIV. *Experiments in Fluids* 55: 1704
- Castro IPaR, A. G. (1977) The flow around a surface-mounted cube in uniform and turbulent streams. *Journal of Fluid Mechanics* 79: 307-335
- Devenport W, Alexander N, Glegg S, and Wang M (2018) The sound of flow over rigid walls. *Annual Review of Fluid Mechanics, Vol 50* 50: 435-458
- Flack KA, and Schultz MP (2014) Roughness effects on wall-bounded turbulent flows. *Physics of Fluids* 26: 101305
- Gao J, and Katz J (2018) Self-calibrated microscopic dual-view tomographic holography for 3D flow measurements. *Optics Express* 26: 16708-16725

- Hong J, Katz J, Meneveau C, and Schultz MP (2012) Coherent structures and associated subgrid-scale energy transfer in a rough-wall turbulent channel flow. *Journal of Fluid Mechanics* 712: 92-128
- Hong JR, Katz J, and Schultz MP (2011) Near-wall turbulence statistics and flow structures over three-dimensional roughness in a turbulent channel flow. *Journal of Fluid Mechanics* 667: 1-37
- Ismail U, Zaki TA, and Durbin PA (2018) Simulations of rib-roughened rough-to-smooth turbulent channel flows. *Journal of Fluid Mechanics* 843: 419-449
- Jeong J, and Hussain F (1995) On the identification of a vortex. *Journal of Fluid Mechanics* 285: 69-94
- Jimenez J (2004) Turbulent flows over rough walls. *Annual Review of Fluid Mechanics* 36: 173-196
- Katz J, and Sheng J (2010) Applications of holography in fluid mechanics and particle dynamics. *Annual Review of Fluid Mechanics* 42: 531-555
- Martinuzzi R, and Tropea C (1993) The flow around surface-mounted, prismatic obstacles placed in a fully developed channel flow (data bank contribution). *Journal of Fluids Engineering* 115: 85-92
- Raupach MR, Antonia RA, and Rajagopalan S (1991) Rough-wall turbulent boundary layers. *Applied Mechanics Reviews* 44: 1-25
- Sheng J, Malkiel E, and Katz J (2008) Using digital holographic microscopy for simultaneous measurements of 3D near wall velocity and wall shear stress in a turbulent boundary layer. *Experiments in Fluids* 45: 1023-1035
- Talapatra S, and Katz J (2012) Coherent structures in the inner part of a rough-wall channel flow resolved using holographic PIV. *Journal of Fluid Mechanics* 711: 161-170
- Talapatra S, and Katz J (2013) Three-dimensional velocity measurements in a roughness sublayer using microscopic digital in-line holography and optical index matching. *Measurement Science & Technology* 24: 024004
- Yakhot A, Lu HP, and Nikitin N (2006) Turbulent flow around a wall-mounted-cube: A direct numerical simulation. *International Journal of Heat and Fluid Flow* 27: 994-1009
- Yang Q, and Wang M (2009) Computational study of roughness-induced boundary-layer noise. *AIAA Journal* 47: 2417-2429
- Yang Q, and Wang M (2013) Boundary-layer noise induced by arrays of roughness elements. *Journal of Fluid Mechanics* 727: 282-317
- Zhang C, Wang J, Blake W, and Katz J (2017) Deformation of a compliant wall in a turbulent channel flow. *Journal of Fluid Mechanics* 823: 345-390